**RESEARCH ARTICLE**

# Kinematic Analysis of Small and Slow-Moving Landslides Using Pleiades-1 Satellite Data

**ETIM EYO[1], MAZLAN HASHIM [2,3], MOHD NADZRI MD REBA[2,3], TEMEL BAYRAK[4], AND HIMAN SHAHABI [5]**

[1]Department of Surveying and Geoinformatics, School of Environmental Technology, Federal University of Technology Minna, Minna 920101, Nigeria
[2]Faculty of Built Environment and Surveying, Universiti Teknologi Malaysia, Johor Bahru 81310, Malaysia
[3]Geoscience and Digital Earth Centre (INSTeG), Research Institute for Sustainable Environment (RISE), Universiti Teknologi Malaysia, Johor Bahru 81310, Malaysia
[4]Faculty of Engineering and Architecture, Department of Geomatics Engineering, Sinop University, 57000 Sinop, Turkey
[5]Department of Geomorphology, Faculty of Natural Resources, University of Kurdistan, Sanandaj 66177-15175, Iran

Corresponding author: Mazlan Hashim (mazlanhashim@utm.my)

**ABSTRACT** Although they may have small velocity values, small slope failures can cause damage to facilities such as roads and pipelines. The main goals of this paper are to detect and map, and quantify the kinematics of small and slow-moving landslides in Kutlugün, Northeastern Turkey. Object-based image analysis (OBIA) and rule-based classification techniques were utilized to detect and map the small and slow-moving landslides. The horizontal displacement of the landslides was investigated using the sub-pixel image correlation method, Cosi-Corr software, and Pleiades-1 images. Kalman filtering method and Real-Time Kinematics-Global Positioning System (RTK-GPS) observations were utilized to formulate a kinematic analysis model for the landslides. A total of 123 small landslides covering an area of approximately 413.332 m$^2$ were detected in the study area. The displacements determined by image correlation compare very well with the RTK-GPS measurements, with a maximum deviation of 0.86 mm. The movement rate of the small landslide from RTK-GPS results ranged from 0.80 – 8.28 mm during the six-month monitoring period. The average displacement value for all the monitoring points is 9.88 mm, while the average movement rate is 3.11 mm during the monitoring period. Compared to the deformation obtained using only the RTK-GPS measurements, the optical image correlation produced a more coherent deformation pattern and more detailed information on the extent and distribution of deformation. The results of the kinematic analysis suggest that the entire body of the small landslide moved slowly during the monitoring period.

**INDEX TERMS** Image correlation, kinematic, Pleiades-1 images, real time kinematics-global positioning system, small and slow-moving landslides.

## I. INTRODUCTION

Landslide is one of the major natural hazards causing significant damage to lives, properties, and infrastructure, particularly in mountainous terrain. One of the main problems faced in landslide studies is the challenge of detecting and assessing the conditions of small failures. Small failures typically require more precise and accurate sensors to enhance the mapping of landslide surface features. The availability

The associate editor coordinating the review of this manuscript and approving it for publication was Manuel Rosa-Zurera.

of the latest generation of very high resolution (VHR) optical satellite images (e.g. RapidEye, QuickBird, Ikonos-2, and Pleiades-1) permits the production of highly informative landslide inventory maps.

This paper was motivated by the existence of small and slow-moving landslides in Kutlugün of Macka, Turkey. The available landslide inventory map for this area shows the existence of 51 landslides with a length of 117 to 995 m [1]. There is no available inventory for small landslides with lengths less than 10 m and areas smaller than 100 m$^2$. These small landslides are often ignored because of their perceived less

severe impact. If not urgently remediated they may escalate and cause damage to facilities such as roads and pipelines.

Slow-moving landslides exhibit seasonal variations in their rate of movement depending on the causal factors [2]. Their displacement rates are extremely slow and very slow (<1.6 m/year) according to the classification proposed by [3]. They generally exhibit active and continuous movements with some fluctuations in displacement rates caused by variations in environmental forces such as earthquakes and rainfall. A good case is the Slumgullion landslide in the United States of America which has been moving slowly with seasonally varying velocities for more than 300 years [4]. Although slow-moving landslides may not necessarily lead to loss of lives, compared to rapid slope movements, they may be precursors for faster and more destructive mass movements and can cause severe disruption to roads, buildings, and other infrastructures. According to the United States Transportation Research Board, the yearly expenditures for the maintenance of small slope failures by the State Department of Transportation were estimated to be over $100 million [5].

It may be difficult to detect the effects of slow-moving landslides as they are usually recognized by cracks or ruptures on ground surfaces or the affected facilities. The detection of slow-moving landslides is also challenging due to difficulties in determining their mechanisms, the exact area vulnerable to landslides, the displacement rate, and the prediction of their future behavior. However, increasing pore-pressure driven by seasonal rainfall is the known mechanic that acts upon slow-moving landslides [6]. It is important to monitor the displacement rates of slow-moving landslides for an improved understanding of the kinematics of the landslide processes and to provide support for decision-makers in land management and hazard assessment. Kinematics provides information on the temporal and spatial forces operating within the landslides, the geometries of the landslide boundary, mechanical properties of soil or rock, conditions of external forcing such as rainfall and earthquake, and the characteristics of future landslide displacements [7].

Due to their complex nature, the displacements of slow-moving landslides can be measured using the widths of the cracks associated with them. The conventional methods employed to determine the displacement of slow-moving landslides are mostly extensometer, inclinometer, total station, and Global Positioning System (GPS). These methods are not economical as they have limitations in spatial coverage, and they are time-consuming and labor-intensive [8]. Among these methods, the GPS technique has been frequently used in periodic and continuous three-dimensional (3D) monitoring of slow-moving landslides [9] and [10]. The deformation information acquired by GPS is point-based and numerous GPS points are required for wider area coverage. This is not economical in terms of time and cost. It is also challenging to deploy GPS in a typical rugged landslide environment, and the possibility of the equipment being damaged during a landslide event. The development

of Real Time Kinematics-Global Positioning System (RTK-GPS) technology with the characteristics of high-precision, low-cost, and simple operation has become a fast, efficient tool in landslide monitoring, but there still exists the problem of heavy field workload.

The accessibility of the difficult mountainous terrain is challenging with the above conventional methods. The recognition of cracking and the determination of crack widths associated with small and slow-moving landslides are often difficult. This is because some cracks may be hidden under debris or sand boils, and some of the visible cracks may not have an obvious cause. Also, the measurement of the crack width requires good skill and judgment, as the width may be overestimated if the sides of the crack have slumped [11]. These challenges can be overcome by using the optical image correlation method to measure the displacement rates of the small and slow-moving landslides.

The correlation of VHR optical satellite images has been used to measure 2-dimensional (2D) displacements (with decimeter accuracy) caused by landslide phenomena on the Earth's surface. QuickBird images were used to compute landslide displacements in different time intervals and determine the movement of the slope slide mass with a yearly displacement of 2.5-20 m [12]. A study to evaluate the performance of the least squares matching (LSM) technique by comparing it with the normalized cross-correlation (NCC) method was carried out using QuickBird satellite images acquired at the La Clapière landslide in France [13]. The results of the study using the signal-to-noise ratios (SNR) gain show comparable enhancement in the accuracy of the estimated displacement when using the LSM technique. Pléiades satellite images were used for landslide displacement measurement with a focus on using minimal ground control requirements and without using external digital elevation models (DEMs) and the largest error of 0.13 m was reported [14]. The findings of the study by [14] show that ground control requirements are useful for precise georeferencing of the digital surface model (DSM) and the displacement maps but have a nominal effect on the absolute values of the determined displacements. A study by [15] explored the potential of using ZY-3 and WorldView-2 images to simultaneously analyze the 2D displacements and strain field of the Xishan landslide in China using digital image correlation technique and recommended the possibility of 3D image correlation in the future.

In this paper, the kinematic analysis of small and slow-moving landslides in Kutlugün, Maçka District, Turkey is presented. The main objectives of this paper are to detect and map, and quantify the kinematics of the small and slow-moving landslides in the study area. In order to accomplish these objectives, the object-based image analysis (OBIA) technique, rule-based classification approach, and Pleiades images were employed to detect and map small and slow-moving landslides using the attribute parameters, namely spectral, texture, spatial, and topography. The correlations

of two Pleiades images were performed to determine the horizontal displacements of the small landslides using the software Co-Registration of Optically Sensed Images and Correlation (Cosi-Corr) [16]. Also, the Kalman filtering technique and Real Time Kinematics-Global Positioning System (RTK-GPS) data were applied to develop a kinematic deformation analysis model, for determining the horizontal displacements and velocity fields of the landslide study area.

## II. MATERIALS AND METHODS

### A. STUDY AREA

The study area is Kutlugün in the Maçka district of Turkey, covering an area of 25 km$^2$ (Fig. 1). The area has a temperate climate in the summers and rainy season normally lasting from September to April. The average annual rainfall of the area is about 830 mm [17]. February is the coldest month with an average temperature of 6.7 °C, while the hottest month is August with an average temperature of 23.2 °C [18]. The topographic components of the area include hillsides, mountains, valleys, and stream channels, and the hydrology of the area is controlled by the activities of the Değirmendere River Basin. The geology of the Kutlugün landslide area consists of weathered andesite-basalt and pyroclastic rocks, with clays developing due to the weathering of the rocks [19]. The type of landslide movement in the study area is translational, and the movement amounts to several centimeters per month [19]. The Kutlugün landslides have contributed to the deformation of the highway, and the destruction of a retaining wall and potable water pipeline in the study area [20].

### B. DATA AND MATERIALS

Table 1 gives the details of the data sets used for the analysis in this paper.

The main causative factor for the Kutlugün landslides was identified as changes in the groundwater level [19]. In order to determine the temporal changes of deformation in the study area, it was important to choose the most appropriate observation periods. The period with the highest rainfall regime was chosen as the most appropriate window for the data acquisition (Fig. 2, [21]). Based on this consideration, RTK-GPS observations were carried out between October 2012 and March 2013 using TUSAGA-Aktif GNSS Network in Turkey. The RTK-GPS data was acquired at almost the same time as the Pleiades-1 image.

### C. METHODOLOGY

The work packages in this paper include the detection and mapping of small and slow-moving landslides in the study area, orthorectification and co-registration, displacement estimation, post-processing, and the kinematic deformation analysis model. The flowchart of the methodology is given in Fig. 3.

#### 1) DETECTION AND MAPPING OF SMALL LANDSLIDES
One of the main goals of this paper is the detection and mapping of small landslides (with lengths less than 10 m and
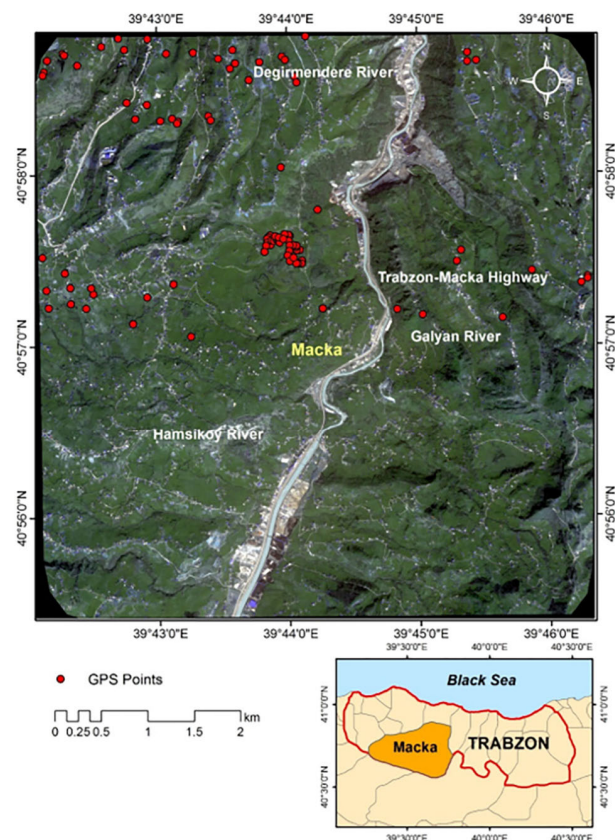


**FIGURE 1.** Pleiades image of study area showing GPS points.

areas smaller than 100 m$^2$) in the study area using Pleiades-1 images and ASTER GDEM. The high spatial resolution multispectral Pleiades-1 imagery was enhanced by combining the panchromatic data with 4-band multispectral data using the Principal Component Analysis (PCA) pan-sharpening module. The semi-automated object-based image analysis (OBIA) and rule-based classification algorithms were utilized to detect and map the small landslide features. These algorithms were implemented in ENVI 5.1 software. The parameters applied in the rule-based classification in this paper were based on spectral, texture, spatial (geometric), and topography attributes. The analysis of these parameters was based on a comparison of small landslides with other surrounding features. The rule-based approach was used to classify the various land cover types in the study area into either landslide or no landslide.

The spectral attributes and the range of values used for the detection of small landslides are given in Table 2. The main spectral parameters employed are the Normalized Difference Vegetation Index (NDVI), the reflectance values, and the Hue, Intensity, and Saturation (HIS).

The gray level co-occurrence matrices (GLCM) were used to analyze textures. The five GLCM parameters commonly employed in texture analysis are contrast, correlation, entropy, standard deviation and mean [22] and [23].

**TABLE 1.** Data used for the study.

| Data | Data/time of acquisition (dd/mm/yyyy) | Mean Across/ Mean along track viewing angle | Mean Across/ Mean along track incidence angle | Solar azimuth/ elevation | Spectral bands | Resolution |
|---|---|---|---|---|---|---|
| Pleiades-1A (Mono) Pleiades-1A (Mono) | 21-10-2012 08:30:15.8 03-04-2013 08:18:20.9 | 15.66/ -12.24 -4.47/ 2.08 | -19.79/ 9.97 5.26/ -1.20 | 168.92/ 37.70 152.73/ 51.66 | PAN: 0.47-0.83 μm (black and white); MS bands: Blue = 0.43-0.55 μm; Green = 0.50-0.62 μm; Red = 0.59-0.71 μm; Near Infrared = 0.74-0.94 μm | PAN = 0.7 m MS = 2.8 m |
| GPS epoch1 GPS epoch2 GPS epoch3 | 24-10-2012 25-01-2013 25-03-2013 | | | | | 5 mm |
| ASTER GDEM | 17-10-2011 | | | | | 30 m |
| SRTM | 11-02-2000 17-04-2013 | (Date acquired) (Date updated) | | | | 30 m |
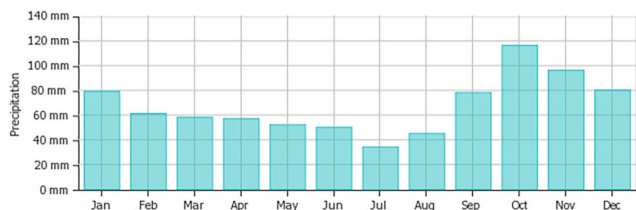


**FIGURE 2.** Average monthly precipitation for the study area in the period (2010-2017).



**FIGURE 3.** Flowchart of methodology.

These attributes and their range of values are given in Table 3. The spatial attributes and the range of their values employed in the detection of small landslides are given in Table 4.

Topography characteristics, namely slope, and elevation were also employed as landslides always occur at high elevations. These topography attributes were generated from a digital elevation model (DEM). In the study area landslides occurred at elevations from 1000 m to 1500 m, with slopes greater than 50%.

### 2) ORTHORECTIFICATION AND CO-REGISTRATION OF SATELLITE IMAGES

Orthorectification and co-registration are the pre-processing steps carried out before the image correlation was performed. Orthorectification is the process of eliminating the effects of image perspective and relief effects to produce a planimetrically correct image. The procedure for orthorectification employs the automatic creation of ground control points (GCPs). Using a raw image (slave) a precise set of GCPs was created based on an already orthorectified image (master). The GCPs were created using an initial rough selection of manually determined tie-points which are iteratively refined. The generated tie-points were filtered and those located in unstable areas (susceptible to displacement) were removed. The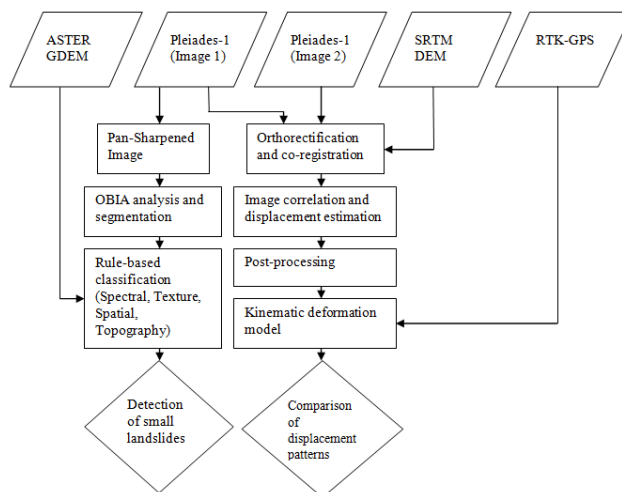 first-order polynomial was used to fit the remaining tie-points and the residuals for each point were computed. A root means square error (RMSE), which represents the scatter of all points about the best fit line, was then determined for the entire fit. All tie-points with high residuals were eliminated, and only those with acceptable RMSE values and suitable distribution and density were utilized.

Ninety-one tie-points were chosen on stable objects in a suitable distribution between ortho-image and raw Pleiades-1 image (21 October 2012). The tie-points were then transformed into GCPs for precise orthorectification. Ten GCPs were utilized and the average misregistration between the ortho-image and Pleiades-1 (3 April 2013) was 15 mm, with a standard deviation of 30 mm. Eighty-seven tie points were also chosen on stable objects in the suitable distribution between this first master ortho-image (from Pleiades-1 image on 21 October 2012) and raw Pleiades-1 image (3 April 2013). Eight GCPs were produced between

**TABLE 2.** Spectral attributes and range of values.

| Feature | Explanation | Bands | Range of values |
|---|---|---|---|
| Reflectance (spectral-mean) | Mean of pixels comprising a segmented object in the blue, green, red or near-infrared band. | Red<br>Green<br>Blue<br>Near-Infrared | 0.058-0.216<br>0.056-0.168<br>0.055-0.102<br>0.120-0.240 |
| NDVI | Ratio of the difference between near-infrared and red reflectance to their sum as an indicator of vegetation greenness. | NDVI (spectral mean) | 0.124-0.361 |
| HIS | Colour space transformation from red-green-blue colour model (RGB) to Hue, intensity and saturation (HIS). | Hue<br>Intensity<br>Saturation | 10-330<br>0.220-0.780<br>0.040-0.340 |

**TABLE 3.** Textural attributes and range of values [22].

| Feature | Equation | Explanation | Range of values |
|---|---|---|---|
| Contrast | $$\sum_{i,j=0}^{N-1} P_{i,j}(i-j)^2$$ | This is a measure of contrast or local intensity. When cell is on the diagonal of the matrix ($i = j$) = 0. | Not Applicable |
| Correlation | $$\sum_{i,j=0}^{N-1} P_{i,j}\left[\frac{(i-\mu_i)(j-\mu_j)}{\sqrt{(\sigma_i^2)(\sigma_j^2)}}\right]$$ | This is a measure of linear dependency of gray-level between pixels at specified positions relative to each other. | Not Applicable |
| Entropy | $$\sum_{i,j=0}^{N-1} P_{i,j}(-\ln P_{i,j})$$ | This is a measure of energy quantity permanently lost to heat when there is a physical transformation. | NDVI (entropy): -11.70 to -11.00 |
| Standard Deviation | Variance:<br>$$\sigma_i^2 = \sum_{i,j=0}^{N-1} P_{i,j}(i-\mu_i)^2; \sigma_j^2 = \sum_{i,j=0}^{N-1} P_{i,j}(j-\mu_j)^2$$<br>Standard Deviation:<br>$$\sigma_i = \sqrt{\sigma_i^2};\ \sigma_j = \sqrt{\sigma_j^2}$$ | This is computed from GLCM variance, which is based on the mean and the dispersion around the mean. | NDVI (Variance): 0.001-0.003 |
| Mean | $$\mu_i = \sum_{i,j=0}^{N-1} i(P_{i,j});\ \mu_j = \sum_{i,j=0}^{N-1} j(P_{i,j})$$ | The GLCM mean is based on the pixel values weighted by the frequency of its occurrence in combination with neighbouring pixel value. | Red band (mean): 0.007-0.180<br>Green band (mean): 0.06-0.15<br>Blue band (mean): 0.06-0.11<br>NIR band (mean): 0.12-0.24<br>NDVI (mean): 0.20-0.40 |

the image pairs and the average misregistration was 10 mm, with a standard deviation of 25 mm. After the generation of accurate GCPs, the computation of the mapping matrices linking ground coordinates with raw pixel coordinates was carried out, to resample the raw image to the orthorectified image.

Co-registration was carried out to precisely align the pre- and post-event images such that when the images were over-laid, the homologous points between the images were at the same location. This process eliminates errors associated with distortions and geo-referencing that remain after orthorectification. In this process, the orthorectification of image spots from the raw slave image was accomplished and their misregistrations with the master image were determined from correlation.

The SRTM 30 m resolution digital elevation model (DEM), prepared by the United States Geological Survey (USGS) was used in the orthorectification and co-registration processes. A digital elevation model is not indispensable when applying Cosi-Corr for image correlation. But in mountainous terrain such as the Kutlugün study area, it was useful to integrate an elevation model to mitigate the effects of topography and distortions during the process of image matching [24].

### 3) DISPLACEMENT ESTIMATION

Several techniques of sub-pixel image correlation have been developed and used in landslide analysis [12] and [25], co-seismic deformation studies [26] and for glacier analysis [27]. In optical image correlation, a pre-event image of the area of interest is compared with a post-event image of the same area. From this comparison, a map of displacements is produced, and the displacement rates can be determined from this map. In this study, the displacements of small and

| Feature | Explanation | Range of values |
|---|---|---|
| Area | Total area of the polygon, minus the area of the holes. | < 100.00 |
| Length | The combined length of all boundaries of the polygon, including the boundaries of the holes. | < 10.00 |
| Compactness | A shape measure that indicates the compactness of the polygon. | < 2.50 |
| Solidity | A shape measure that compares the area of the polygon to the area of a convex hull surrounding the polygon. | < 0.80 |
| Roundness | A shape measure that compares the area of the polygon to the square of the maximum diameter of the polygon. | < 0.50 |
| Elongation | A shape measure that indicates the ratio of the major axis of the polygon to the minor axis of the polygon. | < 2.00 |
| Rectangular-Fit | A shape measure that indicates how well the shape is described by a rectangle. | < 0.60 |

slow-moving landslides were determined using very high-resolution Pleiades-1 satellite images.

Cosi-Corr [16] is the sub-pixel algorithm implemented in this study. It is a robust coarse-to-fine algorithm based on an iterative, unbiased processor that estimates the phase plane using the Fourier algorithm. The software package is a free add-on to the IDL-based module for the remote sensing platform ENVI. Cosi-Corr has a graphical user interface, and the user can define the type of correlator (frequency or statistical) and the size of the correlation window.

The sub-pixel correlation approach employed in this study is the phase correlation. This method is more robust and accurate compared to other classical techniques. The relative displacement between two pre-and post-event images can be derived from the phase difference of the Fourier transform as follows [28] and [29]:

$$i_2(x, y) = i_1(x - \Delta_x, y - \Delta_y) \tag{1}$$

where $i_1$ and $i_2$ are the two images; $\Delta_x$ and $\Delta_y$ are changes in displacement

$$I_2(\omega_x, \omega_y)e^{-j(\omega_x \Delta_x + \omega_y \Delta_y)} \tag{2}$$

where $I_1$ and $I_2$ are the Fourier transform of the two images; $\omega_x$ and $\omega_y$ are the amplitudes of the frequencies.

The expression of the normalised cross power spectrum of images $i_1$ and $i_2$ is given as

$$C_{1,2}(\omega_x, \omega_y) = \frac{I_1(\omega_x, \omega_y) I_2^*(\omega_x, \omega_y)}{|I_1(\omega_x, \omega_y)I_2^*(\omega_x, \omega_y)|} = e^{j(\omega_x \Delta_x + \omega_y \omega_y)} \tag{3}$$

Using the Fourier shift theorem, the relative displacement is given as

$$F^{-1}\{e^{j(\omega_x \Delta_x + \omega_y \Delta_y)}\} = \delta(x + \Delta_x, y + \Delta_y) \tag{4}$$

The first step of the process involves the computation of the pixel displacement between two windows and moving the windows to make allowance for the relative displacement. The subpixel displacement is then determined based on a correlation conducted on the relocated windows. The results include two correlation images: the horizontal ground displacement components (East-West and North-South), and a Signal-to-Noise Ratio (SNR) for each measurement, for assessment of the quality of the results. The accuracy in the measurement of horizontal offsets using Cosi-Corr is in the order of 1/20-1/10 of the pixel size.

### 4) POST-PROCESSING
Post-processing is required to remove (or edit) wrong matches in the displacement field, which are caused by ambiguity and occlusion. The common indices used in the editing process are the signal-to-noise ratio (SNR) and correlation coefficient [30], where low signal-to-noise ratio and low correlation coefficients matched are removed. The displacement estimates are filtered by removing any pixel with SNR values lower than 0.90, thus allowing only displacements from well-correlated chips to remain. More sophisticated post-matching filtering methods were also used for filtering the measurements. Some of the filtering methods include using coherence of the displacement, the displacement direction, the maximum displacement, the maximum cross-correlation coefficient, *etc*. [25]. All these filtering methods require manual tuning of thresholds.

### 5) KINEMATIC DEFORMATION MODEL
Ninety-five (95) GPS points covering the study area and its environment were established to acquire measurements at a specified interval of time. These GPS points were employed to monitor the small landslides. Two periods of RTK-GPS observations of about 2 minutes were acquired at each point (on October 2012, January 2013, and March 2013), and 10-epoch of observations (for every three months) were acquired at each GPS point using TUSAGA-Aktif GNSS Network in Turkey. In order to determine the displacements and velocities of the study area, the analyses were concentrated on the area with a high concentration of small landslides, which consisted of 35 GPS points (see circled area in Fig. 4).

The kinematic deformation model based on the Kalman filtering technique was developed using the adjusted coordinates $X_k, Y_k, Z_k$ of the points and their RMSE $m_{X_K}, m_{Y_K}, m_{Z_K}$ values at the period $k$. Equation (5) below gives the differences of the coordinates between two periods for the object point [19] and [31].

$$\Delta X_{k,k+1} = X_{k+1} - X_k$$
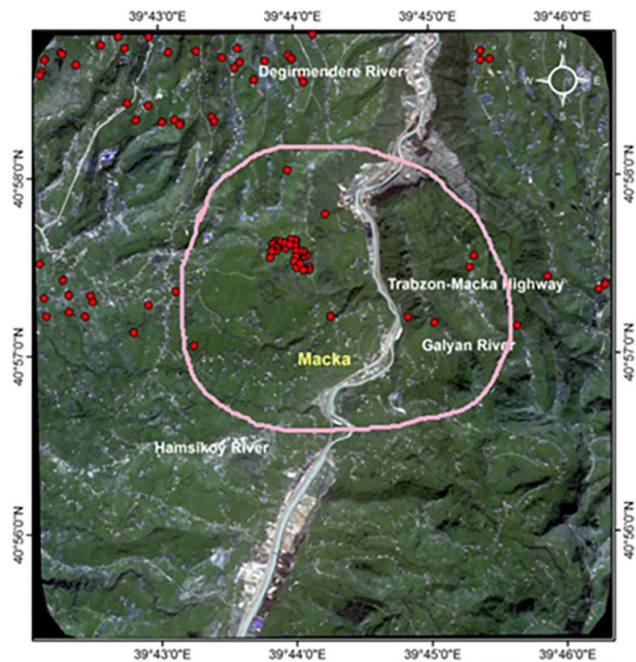$$\Delta Y_{k,k+1} = Y_{k+1} - Y_k$$
$$\Delta Z_{k,k+1} = Z_{k+1} - Z_k \tag{5}$$

**FIGURE 4.** Area with high concentration of small landslides.

Applying the error propagation rule to (5) results to:

$$d\Delta X_{k,k+1} = \frac{\partial \Delta X_{k,k+1}}{\partial X_k} \cdot dX_k + \frac{\partial \Delta X_{k,k+1}}{\partial X_{k+1}} \cdot dX_{k+1}$$

$$d\Delta Y_{k,k+1} = \frac{\partial \Delta Y_{k,k+1}}{\partial Y_k} \cdot dY_k + \frac{\partial \Delta Y_{k,k+1}}{\partial \Delta Y_{k+1}} \cdot dY_{k+1}$$

$$d\Delta Z_{k,k+1} = \frac{\partial \Delta Z_{k,k+1}}{\partial Z_k} \cdot dZ_k + \frac{\partial \Delta Z_{k,k+1}}{\partial \Delta Z_{k+1}} \cdot dZ_{k+1} \quad (6)$$

Re-writing (6) in matrix form gives:

$$\begin{bmatrix} d\Delta X_{k,k+1} \\ d\Delta Y_{k,k+1} \\ d\Delta Z_{k,k+1} \end{bmatrix} = \begin{bmatrix} -1 & 0 & 0 & 1 & 0 & 0 \\ 0 & -1 & 0 & 0 & 1 & 0 \\ 0 & 0 & -1 & 0 & 0 & 1 \end{bmatrix} \cdot \begin{bmatrix} dX_k \\ dY_k \\ dZ_k \\ dX_{k+1} \\ dY_{k+1} \\ dZ_{k+1} \end{bmatrix} \quad (7)$$

The A matrix is given in (8).

$$A = \begin{bmatrix} -1 & 0 & 0 & 1 & 0 & 0 \\ 0 & -1 & 0 & 0 & 1 & 0 \\ 0 & 0 & -1 & 0 & 0 & 1 \end{bmatrix} \quad (8)$$

From (7) the variance and co-variance matrix of the functional model is given as follows:

$$K_{XYZ} = \begin{bmatrix} m_{X_k}^2 & 0 & 0 & 0 & 0 & 0 \\ 0 & m_{Y_k}^2 & 0 & 0 & 0 & 0 \\ 0 & 0 & m_{Z_k}^2 & 0 & 0 & 0 \\ 0 & 0 & 0 & m_{X_{k+1}}^2 & 0 & 0 \\ 0 & 0 & 0 & 0 & m_{Y_{k+1}}^2 & 0 \\ 0 & 0 & 0 & 0 & 0 & m_{Z_{k+1}}^2 \end{bmatrix} \quad (9)$$

Using (7) and (9), a time-dependent kinematic model consisting of displacements and their velocities can be obtained as follows [19] and [31]:

$$X_{k+1} = X_k + (t_{k+1} - t_k)V_{X_k}$$
$$Y_{k+1} = Y_k + (t_{k+1} - t_k)V_{Y_k}$$
$$Z_{k+1} = Z_k + (t_{k+1} - t_k)V_{Z_k}$$
$$V_{X_{k+1}} = V_{X_k}$$
$$V_{Y_{k+1}} = V_{Y_k}$$
$$V_{Z_{k+1}} = V_{Z_k} \quad (10)$$

where: $X_k, Y_k, Z_k$ are the adjusted point coordinates at a time or period $k$, and $V_{X_k}, V_{Y_k}, V_{Z_k}$ are the velocities of point coordinates. The matrix form of (10) also known as the functional model for the kinematic single point model is given in (11) and a shorter form in (12).

$$\bar{Y}_k = \begin{bmatrix} X \\ Y \\ Z \\ V_X \\ V_Y \\ V_Z \end{bmatrix}_{k+1} = \begin{bmatrix} I & I(t_{k+1} - t_k) \\ 0 & I \end{bmatrix} \begin{bmatrix} X \\ Y \\ Z \\ V_X \\ V_Y \\ V_Z \end{bmatrix}_k \quad (11)$$

$$\bar{Y}_k = T_{k,k+1}\hat{Y}_k \quad (12)$$

where: $\bar{Y}_k$: Prediction status (displacements and velocities at period $k$); $\hat{Y}_k$: Status vector at period $k$; $T_{k,k+1}$: Prediction matrix; and $I$: Unit matrix. The prediction state vector at period $k$ and its covariance matrix can be obtained as (13) and (14).

$$\bar{Y}_k = T_{k,k+1}\hat{Y}_k + N_{k,k+1}w_k \quad (13)$$

$$Q_{\bar{Y}\bar{Y},k} = T_{k,k+1}Q_{\hat{Y}\hat{Y},k}T_{k,k+1}^T + N_{k,k+1}Q_{ww,k}N_{k,k+1}^T, \quad (14)$$

where: $N_{k,k+1}$ is the system noise matrix; $w_k$ is the random noise vector at period $k$; $Q_{\bar{Y}\bar{Y},k}$ is the cofactor matrix of status vector and $Q_{ww,k}$ is the cofactor matrix of system noises.

The kinematic model was adjusted and given in matrix form in (15) and (16). The functional model and the stochastic model for the Kalman filtering method are given in (16) and (17), respectively [19] and [31]

$$L_k + V_l = A_k\hat{Y}_k \quad (15)$$

$$\begin{bmatrix} \bar{Y} \\ L_k \end{bmatrix} = \begin{bmatrix} L \\ A_k \end{bmatrix}\hat{Y}_k - \begin{bmatrix} V_{\bar{Y},k} \\ V_{L,k} \end{bmatrix} \quad (16)$$

$$Q_k = \begin{bmatrix} Q_{\bar{Y}\bar{Y},k} & 0 \\ 0 & Q_{LL,k} \end{bmatrix} \quad (17)$$

where: $V$ is the innovation vector; $L_k$ is the actual observation; $A_k\hat{Y}_k$ is the predicted observation. Using (16) and (17), the solution of the kinematic model was determined, and the displacements and velocities were computed based on the two periods of RTK-GPS observations.

## III. RESULTS

### A. DETECTION OF SMALL LANDSLIDES

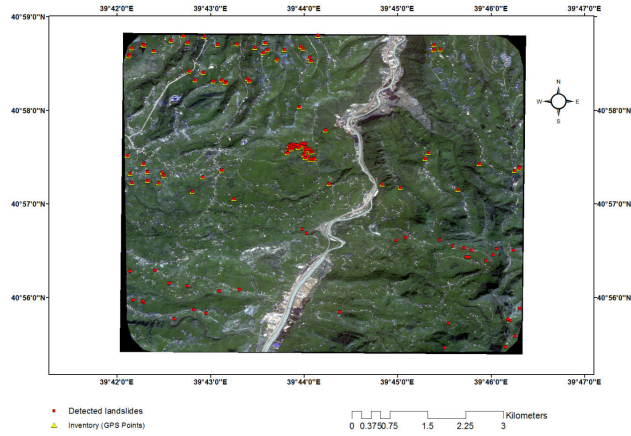The results of the proposed semi-automated object-based methodology for the detection of small landslides are given

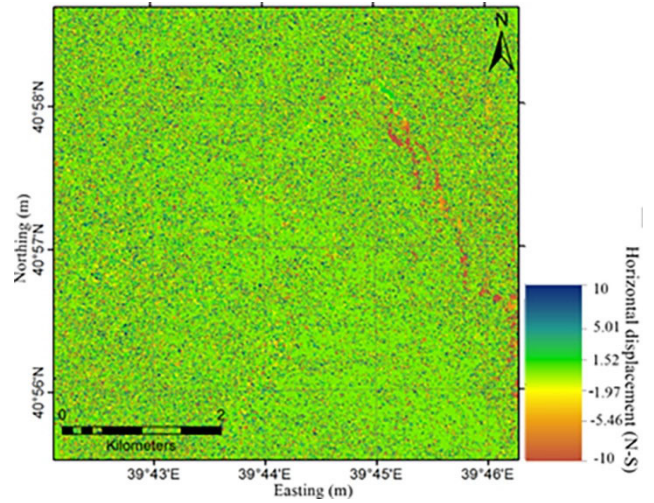**FIGURE 5.** Detected small landslides in the study area.



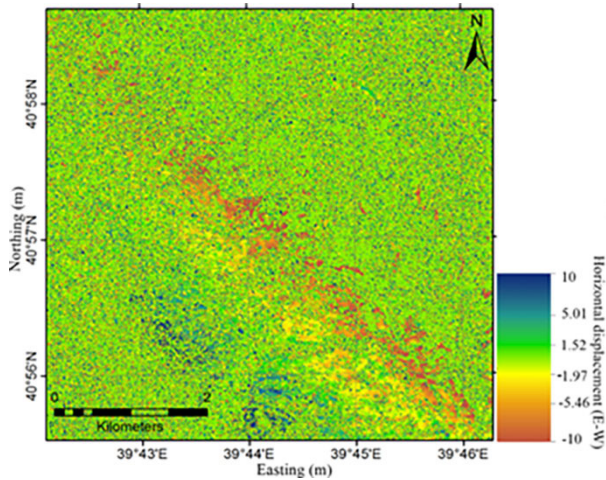**FIGURE 7.** Correlation results (North-South displacement).



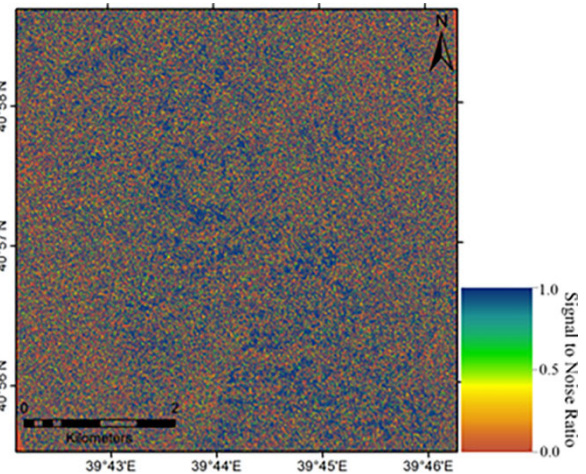**FIGURE 6.** Correlation results (East-West displacement).



**FIGURE 8.** Signal to Noise ratio.

in Fig. 5. A total of 123 small landslides covering a total area of approximately 413.332 m$^2$, were detected in the study area. The inventory map consisting of coordinates of 95 points acquired in the landslides study area using RTK-GPS periodic field surveys was employed to evaluate the accuracy of the proposed methodology for small landslides detection. The accuracy of the detected landslides was realized by using ArcMap 10.3 to compare the observed GPS points with the polygons obtained from the semi-automated OBIA-derived landslides.

The results of the accuracy assessment for detected small landslides in this study produced 81.8% (user's accuracy) and 80.6% (producer's accuracy). An area-based confusion matrix produced the accuracy of the landslide mapping as the user's accuracy (89.8%) and the producer's accuracy (90.4%). The quality percentage (82%) and kappa index (0.87) were high and showed the efficiency of using the proposed methodology for the detection and mapping of small landslides in the study area.

### B. CORRELATION RESULTS

The correlation results consisting of the East-West displacement map, North-South displacement map, and Signal Noise Ratio (SNR), are given in Fig. 6-8. In the image correlation, a chipped window of $128 \times 128$ pixels was used to determine the displacement estimates. The displacements with SNR less than 0.90 were considered decor-related pixels and removed from the results.

For the pre- and post-event images, the difference in angles of the line-of-sight in the East-West direction (mean along track viewing angle) was much greater than the difference in angles of the line-of-sight in the North-South direction (mean across track viewing angle). Thus, the East-West displacements have more noise compared to the North-South displacements. The areas of decorrelation in the East-West displacement map can also be attributed to the presence of clouds in the Pleiades-1 image acquired on 21 October 2012.

The area close to the toe of the landslides also experienced decorrelation due to high displacement rates caused by soil removal.

In the correlation, the SNR generally has high values with an average of 0.95. However, lower SNR values are obtained in areas with low elevation, while relatively high SNR values appear in areas with high elevation. As agricultural activities are mostly concentrated in the mountain foothills, changes can occur in the vegetation cover leading to decorrelation. Thus, there may be unreliability in the displacements detected in this part of the landslide. The valley areas have a lower level of noise after correlation as they have little vegetation with no agricultural activity.

The schematic diagram of the Kutlugün landslide is given in Fig. 9, while the plot of GPS points in the landslide area is given in Fig. 10. The average displacement value (24.04 mm) is highest in the area close to points (Pt. 21, Pt. 22, and Pt. 23) due to the presence of minor quarry activities there. For the area close to the toe of the landslide the average displacement is 9.18 mm, while the area close to the crown section of the landslide has an average displacement of 8.35 mm. Generally, the direction of displacements from optical image correlations is northward (Fig. 11). The circled area in Fig. 11 coincides with the area captured in Fig. 4, 9, and 10.
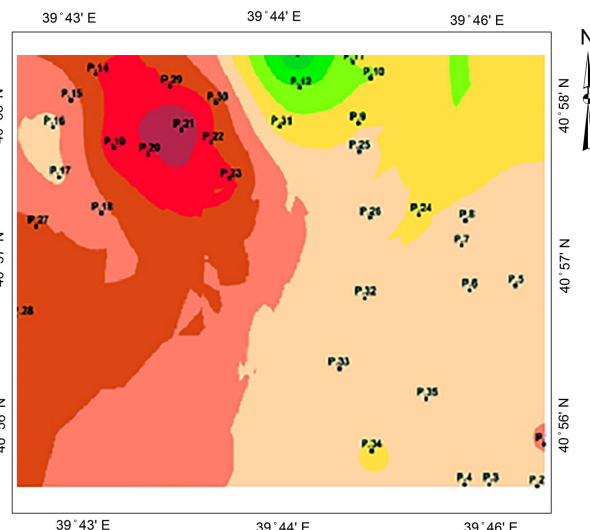


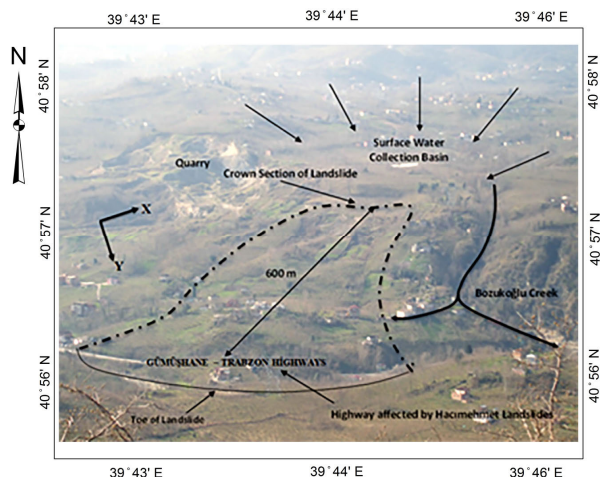FIGURE 10. Observed 35 GPS points in the landslide area.



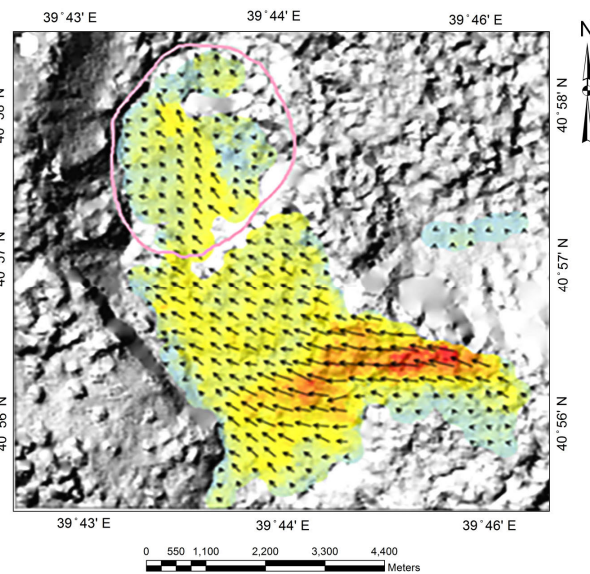FIGURE 9. Schematic diagram of Kutlugün landslide area.



FIGURE 11. Displacement vectors from optical image correlation.

## C. GPS DISPLACEMENTS AND VELOCITIES

The kinematic deformation model based on the Kalman filtering method was implemented in Microsoft Excel. The kinematic analysis was performed using two periods of RTK-GPS observations: October 2012-January 2013 and October 2012-March 2013. The movement parameters of the small landslides include point displacements and their velocities. Tables 5 and 6 show the results of velocities for October 2012-January 2013 and October 2012-March 2013, respectively. The values of velocity were divided by the square-mean errors. Statistical tests were performed by comparing the test values (T) with the t-distribution table values (q).

If velocity values have meaningfully changed, a (+) sign is assigned; alternatively, a (-) sign is assigned. As shown in Tables 5 and 6 almost all the points in the landslide area show significant movements, with varying magnitudes of velocity.

The deformation of GPS points from 24 October 2012 to 25 March 2013 is given in Table 7. The displacement of the small landslides from the RTK-GPS observations varied from 2.77 mm (Pt. 11) to 24.87 mm (Pt. 21) in 6 months, while the velocity varied from 0.80 mm to 8.28 mm/6 months. 31% of the GPS points have displacement values of less than 5 mm, which is largely attributed to the relatively gentle slopes there. 46% of the points have displacement values ranging from 5 - 15 mm. 14% of the points have displacement values ranging from 15 – 20 mm, and 9% of the

**TABLE 5.** Velocity values calculated with kinematic model between october 2012 and january 2013.

| Pt. | Velocities (mm/3Months) | | | Test Values for velocities and decisions (q = 2.04) | | | | | |
|---|---|---|---|---|---|---|---|---|---|
| | $V_{X_k}$ | $V_{Y_k}$ | $V_{Z_k}$ | $T_{X_k}$ | Decision | $T_{Y_k}$ | Decision | $T_{Z_k}$ | Decision |
| 1 | -0.17 | 0.51 | -4.24 | 2.36 | + | 6.85 | + | 38.58 | + |
| 2 | -0.01 | 0.45 | -2.33 | 0.20 | - | 7.05 | + | 22.79 | + |
| 3 | -0.22 | 0.05 | -1.61 | 4.26 | + | 1.00 | - | 15.05 | + |
| 4 | -0.42 | -0.27 | -1.51 | 3.26 | + | 2.12 | + | 6.46 | + |
| 5 | -0.70 | 0.85 | -1.70 | 14.41 | + | 17.46 | + | 13.14 | + |
| 6 | -0.33 | 0.47 | -0.23 | 5.07 | + | 7.07 | + | 2.35 | + |
| 7 | -0.11 | 0.31 | -1.05 | 2.49 | + | 6.38 | + | 10.29 | + |
| 8 | -0.02 | 0.11 | -0.10 | 0.63 | - | 2.36 | + | 1.45 | - |
| 9 | 0.13 | 0.12 | 1.05 | 2.56 | + | 2.35 | + | 7.04 | + |
| 10 | 1.23 | 0.25 | -5.03 | 29.13 | + | 6.00 | + | 50.17 | + |
| 11 | -0.10 | 0.35 | -4.18 | 1.12 | - | 3.53 | + | 26.73 | + |
| 12 | 1.79 | 0.29 | -1.08 | 39.30 | + | 6.63 | + | 11.40 | + |
| 13 | 6.70 | 0.57 | -6.63 | 86.72 | + | 7.45 | + | 30.45 | + |
| 14 | -2.20 | 00.00 | 1.62 | 29.37 | + | 0.09 | - | 10.31 | + |
| 15 | 0.56 | -0.81 | 0.56 | 8.18 | + | 11.65 | + | 4.27 | + |
| 16 | 0.67 | -0.48 | -6.19 | 8.67 | + | 6.30 | + | 45.97 | + |
| 17 | 0.87 | 0.37 | 0.43 | 9.21 | + | 3.99 | + | 3.03 | + |
| 18 | 0.10 | -0.23 | 0.00 | 1.60 | - | 3.59 | + | 0.05 | - |
| 19 | -2.85 | 0.30 | -3.25 | 9.15 | + | 0.99 | - | 5.75 | + |
| 20 | -2.89 | 0.19 | -4.21 | 3.55 | + | 0.25 | - | 2.99 | + |
| 21 | -4.06 | 1.47 | -1.92 | 57.22 | + | 20.69 | + | 14.88 | + |
| 22 | 0.57 | 0.50 | -0.11 | 6.85 | + | 6.01 | + | 1.12 | - |
| 23 | -0.45 | -0.38 | -1.25 | 7.65 | + | 6.52 | + | 6.99 | + |
| 24 | -0.13 | 0.88 | -0.73 | 3.03 | + | 17.29 | + | 14.25 | + |
| 25 | -0.42 | -0.11 | -1.03 | 6.92 | + | 1.89 | - | 10.28 | + |
| 26 | -0.15 | 0.56 | -0.86 | 2.28 | + | 7.71 | + | 6.56 | + |
| 27 | -0.95 | 2.41 | -2.07 | 18.42 | + | 46.59 | + | 12.69 | + |
| 28 | -0.30 | 1.52 | -1.55 | 5.32 | + | 26.15 | + | 11.35 | + |
| 29 | -1.01 | 1.02 | 0.18 | 16.87 | + | 17.03 | + | 1.61 | - |
| 30 | -0.16 | 6.02 | -1.75 | 3.02 | + | 106.39 | + | 13.75 | + |
| 31 | 1.12 | 0.73 | 0.74 | 14.58 | + | 9.53 | + | 4.75 | + |
| 32 | -0.16 | 1.64 | -1.11 | 2.03 | - | 19.51 | + | 5.92 | + |
| 33 | -0.45 | 1.62 | -1.23 | 10.47 | + | 37.66 | + | 12.78 | + |
| 34 | 0.24 | 0.71 | 0.30 | 3.86 | + | 11.05 | + | 1.81 | - |
| 35 | -0.22 | 1.21 | -1.84 | 4.83 | + | 24.76 | + | 15.69 | + |

points (Pt. 21, Pt. 22, and Pt. 23) have displacement values above 20 mm (average value of 23.35 mm). The high displacement values of these points can be ascribed to small quarrying activities close to them. The average displacement value for points close to the toe of the landslide is 8.32 mm, while the average displacement for points close to the crown section of the landslide is 7.58 mm.

Fig. 12 indicates the trends in the directions of movement of the 35 points between October 2012 and January 2013. 23 points (representing 65.7%) moved in the northwest direction; 7 points (representing 20%) moved in the northeast direction; 3 points (representing 8.6%) moved in the southeast direction, and 2 points (representing 5.7%) moved in the southwest direction.

Fig. 13 indicates the trends in the directions of movement of the 35 points between October 2012 and March 2013. 30 points (representing 85%) moved in the northwest

direction, and 5 points (representing 15%) moved in the northeast direction.

These trends show that the landslide movements in the study area are dominantly in the directions of northwest and northeast. The results agree with that of previous work in the study area [19].

### D. COMPARISON OF DISPLACEMENT PATTERNS

The results of optical image correlation are plotted as velocity vectors in Fig. 11, while the results of GPS vector measurements are plotted in Fig. 12 and 13. All the vector plots indicate dominant northward motion. The GPS monitoring results indicate that the movement rate of the small landslide ranged from 0.80 – 8.28 mm during the monitoring period. The average displacement value for all the monitoring points in the study area is 9.88 mm, while the average movement

**TABLE 6.** Velocity values calculated with kinematic model between october 2012 and march 2013.

| Pt. | Velocities (mm/6months) | | | Test Values for velocities and decisions (q = 2.04) | | | | | |
|-----|----------|----------|----------|-----------|----------|-----------|----------|-----------|----------|
| | $V_{X_k}$ | $V_{Y_k}$ | $V_{Z_k}$ | $T_{X_k}$ | Decision | $T_{Y_k}$ | Decision | $T_{Z_k}$ | Decision |
| 1 | -1.04 | 0.70 | -2.77 | 24.49 | + | 16.50 | + | 44.17 | + |
| 2 | -0.7 | 1.3 | -5.4 | 7.66 | + | 5.99 | + | 13.82 | + |
| 3 | -0.72 | 0.75 | -2.31 | 5.30 | + | 8.18 | + | 7.42 | + |
| 4 | -0.85 | 0.41 | -3.54 | 8.93 | + | 4.82 | + | 17.23 | + |
| 5 | -1.73 | 1.17 | -2.87 | 33.21 | + | 22.31 | + | 21.27 | + |
| 6 | -0.52 | 1.42 | -2.54 | 3.95 | + | 10.70 | + | 14.19 | + |
| 7 | -1.18 | 1.25 | -2.07 | 9.99 | + | 9.15 | + | 6.87 | + |
| 8 | -0.26 | 0.85 | -0.73 | 3.20 | + | 7.01 | + | 4.21 | + |
| 9 | -0.57 | 0.69 | -1.30 | 4.53 | + | 5.56 | + | 3.30 | + |
| 10 | 1.46 | 0.50 | -7.09 | 11.90 | + | 4.23 | + | 24.30 | + |
| 11 | -0.49 | 0.63 | -7.56 | 4.97 | + | 4.72 | + | 30.33 | + |
| 12 | 0.48 | 1.09 | -3.95 | 4.54 | + | 10.80 | + | 17.93 | + |
| 13 | 6.12 | 1.93 | -7.83 | 74.85 | + | 24.19 | + | 40.66 | + |
| 14 | -3.85 | 0.77 | 0.00 | 12.94 | + | 7.54 | + | 0.00 | - |
| 15 | -1.29 | 3.24 | -1.27 | 10.61 | + | 26.41 | + | 5.61 | + |
| 16 | -0.49 | 3.19 | -8.94 | 3.05 | + | 19.97 | + | 34.30 | + |
| 17 | -0.47 | 3.22 | -2.06 | 2.16 | + | 15.71 | + | 6.30 | + |
| 18 | -1.49 | 2.79 | -1.52 | 6.32 | + | 9.55 | + | 4.90 | + |
| 19 | -5.09 | 2.46 | -6.17 | 14.55 | + | 11.25 | + | 9.33 | + |
| 20 | -3.45 | 1.75 | -6.78 | 8.11 | + | 14.59 | + | 7.40 | + |
| 21 | -7.09 | 4.28 | -3.65 | 45.01 | + | 27.29 | + | 11.19 | + |
| 22 | -2.08 | 6.28 | -0.77 | 9.59 | + | 29.25 | + | 3.53 | + |
| 23 | -4.47 | 6.72 | -2.88 | 20.86 | + | 31.71 | + | 3.94 | + |
| 24 | 0.19 | 2.04 | -0.34 | 1.21 | - | 9.96 | + | 1.69 | - |
| 25 | -0.88 | 0.68 | -2.67 | 5.87 | + | 5.45 | + | 9.02 | + |
| 26 | -0.61 | 1.43 | -2.14 | 6.03 | + | 11.49 | + | 8.21 | + |
| 27 | -3.06 | 5.42 | -4.44 | 42.31 | + | 74.57 | + | 22.07 | + |
| 28 | -1.86 | 3.61 | -3.28 | 18.29 | + | 33.94 | + | 13.28 | + |
| 29 | -2.67 | 2.14 | 0.63 | 28.44 | + | 22.81 | + | 3.66 | + |
| 30 | -3.61 | 3.91 | -3.53 | 18.36 | + | 17.54 | + | 7.21 | + |
| 31 | 0.56 | 1.85 | -0.79 | 5.47 | + | 18.12 | + | 3.52 | + |
| 32 | -0.63 | 3.50 | -2.41 | 7.95 | + | 37.48 | + | 9.62 | + |
| 33 | -1.31 | 3.56 | -3.53 | 12.68 | + | 33.96 | + | 13.54 | + |
| 34 | 0.04 | 1.59 | -0.48 | 0.40 | - | 14.35 | + | 1.61 | - |
| 35 | -0.09 | 0.25 | -0.36 | 5.50 | + | 14.05 | + | 9.33 | + |
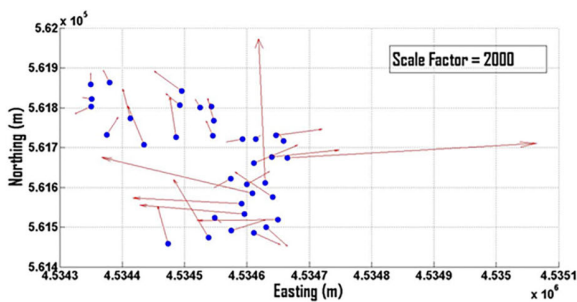


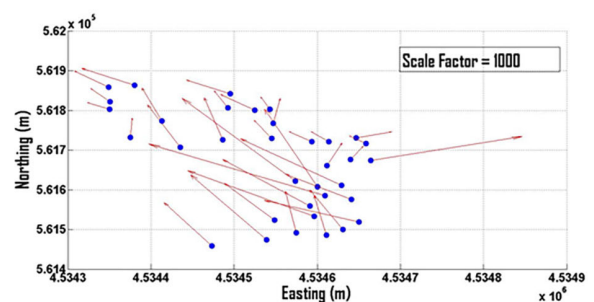**FIGURE 12.** Trends of landslide movements (Oct. 2012 – Jan. 2013).



**FIGURE 13.** Trends of landslide movements (October 2012 – March 2013).

rate is 3.11 mm during the 6-month monitoring period. The RMSE of the overall accuracy of displacement was estimated to be ±0.50 cm.

For the area of largest movement, the average displacement computed from the Pleiades-1 image correlation (24.04 mm) is close to that of the GPS measurements (23.35 mm).

The average displacement values for the area close to the toe of the landslide are 9.18 mm from the optical image correlation and 8.32 mm from the GPS measurements. Also, the average displacement values for the area close to the crown section of the landslide are 8.35 mm from the optical image correlation, and 7.58 mm from the GPS measurements.

**TABLE 7.** Deformation of GPS points from 24 october 2012 to 25 march 2013.

| GPS Pt. | Displacement (mm) | Velocity (mm/6 months) |
|---------|-------------------|------------------------|
| 1 | 7.54 | 1.25 |
| 2 | 5.56 | 1.48 |
| 3 | 3.94 | 1.04 |
| 4 | 3.13 | 0.94 |
| 5 | 6.29 | 2.09 |
| 6 | 4.62 | 1.51 |
| 7 | 5.59 | 1.72 |
| 8 | 3.16 | 0.89 |
| 9 | 3.17 | 0.89 |
| 10 | 4.64 | 1.54 |
| 11 | 2.77 | 0.80 |
| 12 | 3.63 | 1.19 |
| 13 | 19.28 | 6.42 |
| 14 | 12.49 | 3.93 |
| 15 | 10.55 | 3.49 |
| 16 | 9.96 | 3.23 |
| 17 | 10.38 | 3.25 |
| 18 | 10.79 | 3.16 |
| 19 | 18.92 | 5.65 |
| 20 | 15.28 | 3.87 |
| 21 | 24.87 | 8.28 |
| 22 | 20.40 | 6.62 |
| 23 | 24.77 | 8.07 |
| 24 | 6.17 | 2.05 |
| 25 | 3.64 | 1.11 |
| 26 | 4.84 | 1.55 |
| 27 | 18.70 | 6.22 |
| 28 | 12.28 | 4.06 |
| 29 | 10.30 | 3.42 |
| 30 | 16.72 | 5.32 |
| 31 | 5.86 | 1.93 |
| 32 | 10.72 | 3.56 |
| 33 | 11.39 | 3.79 |
| 34 | 4.80 | 1.59 |
| 35 | 8.54 | 2.83 |

The results obtained from these two approaches compare very well, with the deformation pattern obtained from the optical image correlation producing better coherency.

## IV. DISCUSSION

In this paper small and slow-moving landslide objects, which can cause damage to facilities such as roads and buildings, were extracted from segmentation of very high-resolution Pleiades-1 imagery and ASTER GDEM. The landslide recognition parameters were quantified using spectral characteristics of the objects such as NDVI, textural characteristics such as GLCM, spatial characteristics such as area, length, roundness, and elongation, and topography information such as slope and elevation. The developed landslide algorithm was validated in the Kutlugün test site in Northeastern Turkey, and the accuracy assessment of the results showed better landslide detection using the proposed methodology.

While the optical image correlation technique was able to detect small landslide movements in the study area, many factors influenced the quality of the correlation results. The difference in the acquisition angles between the two Pleiades-1 images posed the greatest influence on the correlation results. This influence caused false matches during the correlation process, and thus, the displacement results, especially the East-West displacement map, tended to have more noise. The second influence on the precision of image correlation was the co-registration errors. The RMSE of the tie points was a reliable predictor of correlation precision and the dominant error source. A greater number of tie-points was generated in urban areas with diverse features/textures compared to agricultural areas with similar features/textures. The texture of the area of interest also affected the results of the correlation process [11]. The correlation process produced better results in areas with diverse features/textures.

The results obtained from both image correlation and GPS monitoring show that the landslide has experienced movement with a consistent rate of slow displacement. The fastest displacement was recorded at Pt. 21 and the slowest at Pt. 11.

Given that the GPS observations were carried out during the highest precipitation regime, it is believed that changes in the groundwater level caused by increasing rainfall pattern are the main cause of the Kutlugün landslides.

Although the 35 ground stations monitored with GPS were limited, the monitoring results indicate that the vector directions of the monitoring points were similar to those derived from the image correction. All the monitoring points experienced movement, ranging from 2.77 to 24.87 mm. The quantitative results and the dominant northward trends in the direction of movement suggest that the entire body of the landslide moved as a whole during the 6-month monitoring period.

The movement rates have been quite slow, yet the small and slow-moving landslides have been known to cause damage to the Trabzon-Macka highway and the pipeline conveying drinking water to Trabzon. The materials that form the landslide body consist of mainly weathered andesite-basalt and pyroclastic rocks. The weathering of the rocks has led to the formation of clays, and also resulted in the reduction of the strength of andesite-basalt. The weak constitution of these materials makes them vulnerable to deformation. It can be inferred that local compression, tension, and shearing of the materials caused internal deformation in the landslide body [32]. The release of the internal deformation may have been responsible for the formation of cracks and some minor slides on the road surface.

## V. CONCLUSION

One of the objectives of this paper was to employ the OBIA technique in the detection and mapping of small landslides of less than 100 m$^2$ in area. This is the first time that the OBIA algorithm is being developed to quantify the attribute parameters of small translational landslides that distinguishes them from other surrounding features. This is also the first time that the Pleiades-1 image is being employed to develop metrics for the detection and mapping of small landslides. The landslide inventory map produced in the study will constitute a benchmark for future mapping of small landslides in the study area.

The kinematics of small and slow-moving Kutlugün landslide was also investigated based on quantitative analysis of VHR Pleiades images of October 2012-April 2013 and GPS monitoring data for October 2012-March 2013 period. The comparison of results for optical image correlation and GPS measurements was better in areas consisting of diverse features/textures such as urban areas than in areas with similar features/textures such as agricultural fields. In all, the displacement detected by Cosi-Corr compares very well with the GPS measurements, with a maximum deviation of 0.86 mm. However, some discrepancies were detected in the optical image correlation results due to decorrelation caused by differences in the viewing angles and the presence of clouds in the Pleiades-1 images. Compared to the deformation obtained solely using GPS measurements, the deformation pattern produced from the optical image correlation was more coherent.

Also, the results of image correlation yielded a bigger density of vectors which produced more comprehensive information on the extent and distribution of deformation.

The analysis of the kinematics results suggests that the entire body of the small landslide moved slowly during the 6-month monitoring period. Based on the kinematic results, it is inferred that the small landslide is largely influenced by the steep mountainous terrain and the rainfall regime. The results of this study will provide vital tools for engineers and planners to mitigate hazards and manage disasters associated with small and slow-moving landslides on infrastructure.

The precision of optical image correlation is largely influenced by the coregistration process. The suggestions to improve the co-registration process may include the development of algorithms for the automatic generation of tie-points, and the formulation of improved approaches to evaluate the quality of the tie-points. Also, given that the GPS monitoring data used to validate the optical image correlation results were acquired during the highest rainfall period, it is believed that the main causal factor of the small landslides is increased rainfall. However, for future study, it is important to also acquire GPS data during low rainfall periods to investigate the correlation between rainfall and displacement in the study area.

The efficient performance of optical image correlation in measuring horizontal displacements provides a platform to create a detailed database of small landslides in the study area. This database can be employed by engineers and planners to analyze the complex mechanics of small and slow-moving landslides for an improved theoretical understanding of their mechanisms [11]. Also, this database can be utilized by researchers as input data to calibrate existing empirical models and produce comprehensive empirical models to predict the future spread of small landslides.

While landslides in the study area have been previously monitored using only periodic and real-time GPS observations, for the first time this study performs rigorous analyses of movement characteristics of small and slow-moving landslides in the study area using optical image correlation and GPS monitoring data. The techniques developed in this study have wide applications which can be efficiently utilized to measure slow deformation in different surface processes such as sand dunes migration and glacier flow. Further developments of this study may involve the analysis of additional datasets using Synthetic Aperture Radar Interferometry (InSAR) techniques, as their high sensitivity can provide a useful contribution to the understanding of landslide behavior and dynamics [33].

## REFERENCES

[1] T. Kavzoglu, E. K. Sahin, and I. Colkesen, "Selecting optimal conditioning factors in shallow translational landslide susceptibility mapping using genetic algorithm," *Eng. Geol.*, vol. 192, pp. 101–112, Jun. 2015, doi: 10.1016/j.enggeo.2015.04.004.

[2] B. Gündoğdu, "Relations between pore water pressure, stability and movements in reactivated landslides," MSc thesis, Dept. Civil Eng, Middle East Tech. Univ., Ankara, Turkey, 2011, p. 115.

[3] D. M. Cruden and D. J. Varnes, "Landslide types and processes," in *Landslides and Engineering Practice*, A. K. Turner and R. L. Schuster Eds. Washington, DC, USA: Transportation Research Board, Jun. 1996, pp. 36–75.

[4] J. A. Coe, W. L. Ellis, J. W. Godt, W. Z. Savage, J. E. Savage, J. A. Michael, J. D. Kibler, P. S. Powers, D. J. Lidke, and S. Debray, "Seasonal movement of the Slumgullion landslide determined from global positioning system surveys and field instrumentation, July 1998-March 2002," *Eng. Geol.*, vol. 68, pp. 67–101, Feb. 2003, doi: 10.1016/S0013-7952(02)00199-0.

[5] L. J. Schmidt. *When Landslides*. Accessed: Mar. 12, 2021. [Online]. Available: https://www.earthobservatory.nasa.gov/Features/Landslide

[6] A. L. Handwerger, J. J. Roering, and D. A. Schmidt, "Controls on the seasonal deformation of slow-moving landslides," *Earth Planet. Sci. Lett.*, vols. 377–378, pp. 239–247, Sep. 2013, doi: 10.1016/j.epsl.2013.06.047.

[7] W. H. Schulz, J. A. Coe, P. P. Ricci, G. M. Smoczyk, B. L. Shurtleff, and J. Panosky, "Landslide kinematics and their potential controls from hourly to decadal timescales: Insights from integrating ground-based InSAR measurements with structural maps and long-term monitoring data," *Geomorphology*, vol. 285, pp. 121–136, May 2017, doi: 10.1016/j.geomorph.2017.02.011.

[8] M. F. Mansour, N. R. Morgenstern, and C. D. Martin, "Expected damage from displacement of slow-moving slides," *Landslides*, vol. 8, no. 1, pp. 117–131, Mar. 2011, doi: 10.1007/s10346-010-0227-7.

[9] G.-Q. Wang, "Kinematics of the Cerca del Cielo, Puerto Rico landslide derived from GPS observations," *Landslides*, vol. 9, no. 1, pp. 117–130, Mar. 2012, doi: 10.1007/s10346-011-0277-5.

[10] R. Xiao, X. He, and L. Li, "Continuous monitoring of landslide and atmospheric water vapour using GPS: Applications in Pubugou hydropower resettlement zone," in *Proc. China Satell. Navigat. Conf. (CSNC)*, in Lecture Notes in Electrical Engineering, Guanzhou, China, May 2012, pp. 305–313.

[11] J. G. Martin, "Measuring liquefaction-induced deformation from optical satellite imagery," MSc thesis, Dept. Civil Eng., Univ. Texas Austin, TX, USA, 2014, p. 153.

[12] C. Delacourt, P. Allemmand, B. Casson, and H. Vadon, "Velocity field of the 'La Clapière' landslide measured by the correlation of aerial and QuickBird satellite images," *Geophys. Res. Lett.*, vol. 31, no. 15, pp. 1–5, 2004, doi: 10.1029/2004GL020193.

[13] M. Debella-Gilo and A. Kääb, "Measurement of surface displacement and deformation of mass movements using least squares matching of repeat high resolution satellite and aerial images," *Remote Sens.*, vol. 4, no. 1, pp. 43–67, Jan. 2012, doi: 10.3390/rs4010043.

[14] A. Stumpf, J.-P. Malet, P. Allemand, and P. Ulrich, "Surface reconstruction and landslide displacement measurements with Pléiades satellite images," *ISPRS J. Photogramm. Remote Sens.*, vol. 95, pp. 1–12, Sep. 2014, doi: 10.1016/j.isprsjprs.2014.05.008.

[15] B. Shi, C. Liu, H. Wu, and P. Lu, "Elementary analysis of the mechanism of Xishan landslide based on pixel tracking on VHR images," *Int. J. Geohazards Environ.*, vol. 2, no. 2, pp. 53–71, 2016, doi: 10.15273/ijge.2016.02.007.

[16] S. Leprince, S. Barbot, F. Ayoub, and J.-P. Avouac, "Automatic and precise orthorectification, coregistration, and subpixel correlation of satellite images, application to ground deformation measurements," *IEEE Trans. Geosci. Remote Sens.*, vol. 45, no. 6, pp. 1529–1558, Jun. 2007, doi: 10.1109/TGRS.2006.888937.

[17] T. Kavzoglu, E. K. Sahin, and I. Colkesen, "Landslide susceptibility mapping using GIS-based multi-criteria decision analysis, support vector machines, and logistic regression," *Landslides*, vol. 11, no. 3, pp. 425–439, Jun. 2014, doi: 10.1007/s10346-013-0391-7.

[18] A. Yalcin, S. Reis, A. C. Aydinoglu, and T. Yomralioglu, "A GIS-based comparative study of frequency ratio, analytical hierarchy process, bivariate statistics and logistics regression methods for landslide susceptibility mapping in Trabzon, NE Turkey," *CATENA*, vol. 85, no. 3, pp. 274–287, Jun. 2011, doi: 10.1016/j.catena.2011.01.014.

[19] M. Yalçinkaya and T. Bayrak, "Comparison of static, kinematic and dynamic geodetic deformation models for Kutlugün landslide in northeastern Turkey," *Natural Hazards*, vol. 34, no. 1, pp. 91–110, Jan. 2005, doi: 10.1007/s11069-004-1967-2.

[20] M. Yalçinkaya, T. Bayrak, and A. Yalçin, "Modelling landslide surfaces by kinematic and dynamic surface models: A case study in north eastern Turkey," *Surv. Rev.*, vol. 38, no. 297, pp. 229–242, Jul. 2005, doi: 10.1179/sre.2005.38.297.229.

[21] Accessed: May 5, 2020. [Online]. Available: http://www.weather-and-climate.com

[22] M. Hall-Beyer. *GLCM: A Tutorial, Version 3.0*. Accessed: Apr. 5, 2020. [Online]. Available: https://www.researchgate.net/publication/315776784_GLCM_Texture_A_Tutorial_v_30_March_2017

[23] T. Blaschke, B. Feizizadeh, and D. Holbling, "Object-based image analysis and digital terrain analysis for locating landslides in the Urmia Lake Basin, Iran," *IEEE J. Sel. Topics Appl. Earth Observ. Remote Sens.*, vol. 7, no. 12, pp. 4806–4817, Dec. 2014, doi: 10.1109/jstars.2014.2350036.

[24] F. Ayoub, S. Leprince, and J.-P. Avouac, "Co-registration and correlation of aerial photographs for ground deformation measurements," *ISPRS J. Photogramm. Remote Sens.*, vol. 64, no. 6, pp. 551–560, Nov. 2009, doi: 10.1016/j.isprsjprs.2009.03.005.

[25] M. Debella-Gilo and A. Kääb, "Sub-pixel precision image matching for measuring surface displacements on mass movements using normalized cross-correlation," *Remote Sens. Environ.*, vol. 115, no. 1, pp. 130–142, Jan. 2011, doi: 10.1016/j.rse.2010.08.012.

[26] J. Hollingsworth, S. Leprince, F. Ayoub, and J.-P. Avouac, "Deformation during the 1975–1984 Krafla rifting crisis, NE iceland, measured from historical optical imagery," *J. Geophys. Research: Solid Earth*, vol. 117, no. B11, pp. 1–24, Nov. 2012, doi: 10.1029/2012JB009140.

[27] T. Heid and A. Kääb, "Repeat optical satellite images reveal widespread and long term decrease in land-terminating glacier speeds," *Cryosphere*, vol. 6, no. 2, pp. 467–478, Apr. 2012, doi: 10.5194/tc-6-467-2012.

[28] H. S. Stone, M. T. Orchard, E.-C. Chang, and S. A. Martucci, "A fast direct Fourier-based algorithm for subpixel registration of images," *IEEE Trans. Geosci. Remote Sens.*, vol. 39, no. 10, pp. 2235–2243, Oct. 2001, doi: 10.1109/36.957286.

[29] H. Foroosh, J. B. Zerubia, and M. Berthod, "Extension of phase correlation to subpixel registration," *IEEE Trans. Image Process.*, vol. 11, no. 3, pp. 188–200, Mar. 2002, doi: 10.1109/83.988953.

[30] D. J. Quincey and N. F. Glasser, "Morphological and ice-dynamical changes on the Tasman Glacier, New Zealand, 1990–2007," *Global Planet. Change*, vol. 68, no. 3, pp. 185–197, Aug. 2009, doi: 10.1016/j.gloplacha.2009.05.003.

[31] M. Acar, M. T. Ozludemir, S. Erol, R. N. Celik, and T. Ayan, "Kinematic landslide monitoring with Kalman filtering," *Natural Hazards Earth Syst. Sci.*, vol. 8, no. 2, pp. 213–221, Mar. 2008, doi: 10.5194/NHESS-8-213-2008.

[32] S. Jiang, B.-P. Wen, C. Zhao, R.-D. Li, and Z.-H. Li, "Kinematics of a giant slow-moving landslide in Northwest China: Constraints from high resolution remote sensing imagery and GPS monitoring," *J. Asian Earth Sci.*, vol. 123, pp. 34–46, Jun. 2016, doi: 10.1016/j.jseaes.2016.03.019.

[33] K. O. Hastaoglu, "Comparing the results of PSInSAR and GNSS on slow motion landslides, Koyulhisar, Turkey," *Geomatics, Natural Hazards Risk*, vol. 7, no. 2, pp. 786–803, Nov. 2014, doi: 10.1080/19475705.2014.978822.

**ETIM EYO** was born in Ituk Mbang, Nigeria. He received the B.Sc. degree in land surveying from Ahmadu Bello University, Zaria, Nigeria, in 1994, the M.Sc. degree in surveying and geoinformatics from the University of Lagos, Nigeria, in 2002, and the Ph.D. degree in geomatic engineering from Universiti Teknologi Malaysia (UTM), Malaysia, in 2020.

He is currently the Head of the Department of Surveying and Geoinformatics, Federal University of Technology, Minna, Nigeria. He has more than 20 years of teaching/research experience in the universities (and collaboration with industries) in Nigeria, Malaysia, Turkey, and England. He is an expert in geomatic engineering, specializing in the application of satellite remote sensing technologies, global positioning systems, geographic information systems, and numerical and computational modeling techniques for the optimization of decision-making in environmental resource management operations.

Dr. Eyo is a Registered Surveyor by the Surveyors Council of Nigeria (SURCON).

**MAZLAN HASHIM** was born in Johore, Malaysia. He received the bachelor's degree in surveying (land) from Universiti Teknologi Malaysia (UTM), in 1984, the M.Sc.Eng. degree in surveying engineering from the University of New Brunswick, Canada, in 1987, and the Ph.D. degree in remote sensing from the University of Stirling, U.K., in 1995.

He is currently a Professor of remote sensing with the Faculty of Built Environment and Surveying and a Senior Research Fellow with the Geoscience and Digital Earth Centre (INSTeG), UTM. He is an expert in satellite remote sensing data processing and modeling for mapping and environmental applications. He has published his research works in more than 130 high-impact articles indexed in SCOPUS and Web of Science, with H-index of 37.

Prof. Hashim is a Fellow of the Academy Sciences Malaysia and the Institution of Geospatial and Remote Sensing Malaysia.

**MOHD NADZRI MD REBA** received the B.Sc. degree in remote sensing from Universiti Teknologi Malaysia (UTM), in 2002, the M.Sc. degree in photogrammetry and geoinformatics from the Stuttgart University of Applied Science, Germany, in 2005, and the Ph.D. degree in signal theory and communications and the Diploma of Advance Engineering (DEA) degree from Universitat Politécnica de Catalunya (UPC), Spain, in 2010. He is currently an Associate Professor with the Faculty of Built Environment and Surveying and the Director of the Geoscience and Digital Earth Centre (INSTeG). He has published papers in many national and international journals. His research interests include remote sensing, microwave, optical sensing, and machine learning.

**TEMEL BAYRAK** was born in Trabzon, Turkey. He received the Ph.D. degree in geodesy and photogrammetry engineering from Karadeniz Technical University, Trabzon, in 2003.

He is currently a Professor of geomatics engineering with Sinop University, Turkey. He has published and refereed papers in many national and international journals. His research interests include geodesy, satellite positioning and navigation, engineering surveying, adjustment computation, and computer programming.

**HIMAN SHAHABI** received the Ph.D. degree in remote sensing-GIS from the Department of Remote Sensing, Faculty of Geoinformation and Real Estate, and the Ph.D. degree in remote sensing-GIS from the Institute of Geoscience and Digital Earth Centre (Geo-DEC), Research Institute for Sustainability and Environment (RISE), Universiti Teknologi Malaysia (UTM), Malaysia.

He is currently an Associate Professor of remote sensing with the Department of Geomorphology (Remote Sensing/GIS), Faculty of Natural Resources, University of Kurdistan, Sanandaj, Iran. He has published his research works in more than 120 high-impact articles indexed in SCOPUS and Web of Science, with H-index of 58. His research interests include image processing, GIS application, soft computing techniques in natural hazards, and geosciences. He served as an Associate Editor and a Reviewer for the board of journals, like *Geographic Information System Modeling*, *Remote Sensing*, *Natural Hazards*, and *Machine Learning*.

● ● ●